Applied Physics A (2021) 127:334
https://doi.org/10.1007/s00339-021-04476-y

Applied Physics A
Materials Science & Processing

Numerical studies of dielectric material modifications by a femtosecond Bessel–Gauss laser beam

R. Beuton[1] · B. Chimier[1] · P. Quinoman[1] · P. González Alaiza de Martínez[1] · R. Nuter[1] · G. Duchateau[1]

Received: 21 December 2020 / Accepted: 29 March 2021 / Published online: 12 April 2021
© The Author(s), under exclusive licence to Springer-Verlag GmbH, DE part of Springer Nature 2021

Abstract
Femtosecond Bessel–Gauss beams are attractive tools to a large area of laser processes including high aspect ratio volume nanostructuration in dielectric materials. Understanding the dielectric material response to femtosecond Bessel–Gauss beam irradiation is key in controlling its modifications and designing new structures. In this work, we show how the material ionization affects the propagation of the femtosecond Bessel–Gauss laser beam and can limit the laser energy deposition. By performing 2D/3D numerical simulations, we evaluate the absorbed laser energy and subsequent material modifications. First, we model the electron dynamics in the material coupled to the 3D laser propagation effects. Then, we consider 2D thermo-elasto-plastic simulations to characterize the medium modifications. Results show that the laser ionized matter induces a screening of the incident gaussian beams which form the Bessel-Gauss beam. This effect leads to a limitation of the maximum laser energy deposition even if the incident laser energy increases. It can be reduced if a tigthly focused femtosecond Bessel–Gauss beam is used as the angular aperture of the cone along which the incident gaussian beams are distributed is larger.

Keywords Laser-dielectric interaction · Bessel beams · Femtosecond laser pulse · Dielectric structuration

1 Introduction

Femtosecond laser pulse is a versatile tool for processing of dielectric materials [1–4] due to a highly nonlinear laser energy absorption and an irradiation time shorter than typical hydrodynamic and thermal relaxation times in dielectrics (~ 10 ps). This fast heating process provides an efficient way to induce material modifications in the bulk of dielectrics and has numerous applications in many fields, such as photonics or micromachining [5]. But, the size of laser induced structures is limited by the focal volume which is small for traditionnal Gaussian pulses as they must be tightly focused inside the dielectric [6, 7]. This limitation can be overcome by using non-diffractive Bessel–Gauss beams. These beams correspond to long and narrow filaments along the optical axis with only hundreds of nanometers in diameter, and a length which may exceed several hundreds of microns [8–10].

A Bessel–Gauss beam is usually produced by using axicon and results from interferences of incident Gaussian beam with itself [11, 12]. The laser pulse energy propagates along directions distributed on a cone surface with a given angle θ with the axial propagation direction, and converge to a line. For dielectric material modifications, the formed Bessel–Gauss beam is then projected inside the matter by a $4f$ afocal imaging system [13, 14] and on-axis intensity may be tailored by using spacial light modulators or filters [15, 16]. For this kind of nonpropagative beam, as the laser energy does not propagate on propagation axis, it is generally assumed that the laser energy can be absorbed in the matter along the whole length of the imaged beam. Depending on the incident laser energy, modifications in the whole irradiated volume, like refractive index variation or void structure formation, can be obtained [1–3, 17], which is of interest for high aspect ratio, uniform, and submicron structuring of transparent materials by using a single laser pulse. However, for femtosecond Bessel–Gauss laser pulses, void structures in bulk of fused silica can be achieved only in tight focusing conditions [3, 18]. A large θ value leading

✉ B. Chimier
benoit.chimier@u-bordeaux.fr

[1] Centre Lasers Intenses et Applications, Université de Bordeaux - CNRS - CEA, UMR 5107, 33405 Talence, France

to a Bessel–Gauss beam core of submicrometer full width at half–maximum is necessary. An influence of the optical material response (optical index change inducing diffraction, plasma screening, etc) has been suggested to affect the laser pulse propagation and limit the laser energy deposition. This effect is assumed to decrease since the θ value increases. Understanding this limitation of laser energy absorption is therefore necessary to control and improve material processing by using femtosecond Bessel–Gauss beams.

To understand and explain such experimental observations in femtosecond regime, material modifications in fused silica by 60 fs and 800 nm Bessel–Gauss laser pulses are numerically studied in the present work. These laser parameters correspond to those used in [3, 18]. Three different θ values are considered to evaluate the influence of the Bessel–Gauss beam diameter. Due to the different timescales involved during the material modification, electron dynamics including laser energy absorption and electron energy transfer toward the lattice can be decoupled from hydrodynamic processes and thermal conduction [7]. The electron dynamics coupled to the propagation of Bessel–Gauss beam is widely modeled by solving the nonlinear Schrödinger equation supplemented with a rate equation describing ionization and recombination of conduction band electrons [2, 14, 19]. However, the nonlinear Schrödinger equation is based on approximations of slowly varying envelope of laser pulse and light scattering limited to small angles. These assumptions are valid as long as the conduction electron density in the irradiated matter remains lower than the critical density during the laser pulse propagation, that means to moderate laser intensities for which only small modifications are expected. In this work, to address the formation of cavity or channel inside dielectric material which require high intensities and possibly electron densities in excess of the critical density, full Maxwell's equations coupled to the electron dynamics are used to model the laser pulse propagation and interaction. A two temperature fluid model including ionization processes has been introduced in a 3D Maxwell solver (ARCTIC code [20]) and is presented in Sect. 2. The evolution of the electron dynamics and laser energy deposition in the bulk are studied in Sect. 3 for femtosecond Bessel–Gauss beams with different beam diameters. Influence of the material ionization on the Bessel–Gauss laser beam formation is shown and discussed. A limitation of the maximum material laser heating depending of the beam diameter is observed. The calculated absorbed energy profile is then used as initial condition in the hydrodynamic code CHIC [21] including the elasto–plastic behavior of the solid matter [22–24]. It provides material modifications post to the interaction, which are presented in Sect. 4. In agreement with experimental results [3, 18], the smaller the Bessel–Gauss beam diameter (tighter focusing condition), the stronger the material modification.

2 Modeling of laser propagation and energy deposition

The Maxwell's equations for the laser pulse propagation through a dielectric medium read:

$$\begin{aligned} &\boldsymbol{\nabla} \wedge \mathbf{E} = -\partial_t \mathbf{B} \quad \text{and} \\ &\mu_0^{-1} \boldsymbol{\nabla} \wedge \mathbf{B} = \partial_t \mathbf{D} + \mathbf{J}, \end{aligned} \tag{1}$$

where $\mathbf{E}$, $\mathbf{D}$, $\mathbf{B}$, and μ_0 are the laser electric field, the electric displacement field, the magnetic field, and the vacuum permeability, respectively. The current $\mathbf{J} = \mathbf{J}_I + \mathbf{J}_e$, where $\mathbf{J}_I$ is the effective ionization current depending on the material bandgap and photoionization rate [25] **and** $\mathbf{J}_e = -en_e\mathbf{u}_e$ is the free electron current density (n_e and $\mathbf{u}_e$ are the conduction electron density and velocity, respectively). The electric displacement field $\mathbf{D}$ accounts for material polarization through linear and nonlinear dielectric susceptibilities [25] $\chi^{(1)}$ and $\chi^{(3)}$, respectively.

The electron dynamics in the conduction band and lattice heating are described by using a two–temperature fluid model assuming isochoric processes and neglecting thermal conduction. The electron momentum equation is written as

$$\partial_t \mathbf{u}_e = -e\mathbf{E}/m_e - \mathbf{u}_e \nu_e, \tag{2}$$

where m_e is the electron mass, and ν_e is the effective electron collision frequency. The evolution of the electron density in the conduction band is given by

$$\partial_t n_e = W_{PI} + W_{Col} - n_e/\tau_r, \tag{3}$$

where the last term accounts for the electron decay with the characteristic time τ_r, the photoionization rate W_{PI} is given by the Keldysh expression for solids [26], and the impact ionization rate W_{Col} is evaluated by [27, 28]

$$W_{Col} = \alpha_0 \int \left(\frac{\varepsilon}{U_g} - 1 \right)^2 f_e(\varepsilon) d\varepsilon, \tag{4}$$

where α_0 is a constant rate depending on material, U_g is the material bandgap, and f_e is the electron energy distribution which is assumed to be a Maxwellian in this study.

The internal electron energy ξ_e is given by

$$\partial_t(n_e\xi_e) = n_e m_e u_e^2 \nu_e - (3/2)U_g W_{Col} - \gamma_{el}(T_e - T_l), \tag{5}$$

where the two last terms represent the energy lost due to collisional ionization and to the lattice heating process, respectively. $\gamma_{el} = 3n_e k_B/(2\tau_{el})$ is the electron-lattice coupling where τ_{el} is the electron-lattice relaxation time, and T_e and T_l are the electron and lattice temperatures ($T_e = 2\xi_e/(3k_B)$). The lattice temperature evolution is given by

$$C_l \partial_t T_l = \gamma_{el}(T_e - T_l), \tag{6}$$

where C_l is the lattice heat capacity.

The previous equations are implemented in the code ARCTIC [20], where Maxwell Eq. (1) are discretized in the three spatial dimensions by means of Yee scheme [29]. The simulation domain includes Bérenger's Perfectly-Matched-Layer absorbing boundary condition [30, 31]. The propagation axis is x.

Instead of determining the initial boundary conditions by simulating all the imaging system to produce a Bessel–Gauss beam, the analytical expression given in Ref. [32] has been used. This expression corresponds to a Bessel–Gauss beam generated by using an annular aperture as filter [15, 16]. In vacuum, the beam intensity is maximum in $x = 0$, and

$$\mathbf{E}(x = 0, r, t) = \mathbf{E}_0(t) J_0(\beta r) \exp\left[-(r/w_0)^2\right], \tag{7}$$

where J_0 corresponds to the zero order Bessel function, $\mathbf{E}_0(t)$ includes the Gaussian temporal dependences, $r = \sqrt{y^2 + z^2}$ and $\beta = k \sin\theta$, θ being the angular half aperture of the cone along which the incident gaussian beams are distributed, and $k = 2\pi/\lambda_l$ (λ_l is the laser wavelength in vacuum). The Bessel–Gauss beam length is given by $D = 2w_0/\tan\theta$. From the electric field defined by Eq. (7), the initial boundary conditions at $x = -25$ μm in simulations are calculated by using the algorithm presented in Ref. [33, 34].

3 Bessel–Gauss beam propagation in bulk of fused silica

For simulation purpose, 60 fs and 800 nm incident laser pulses are considered with maximum peak intensities I_0 at $x = 0$ between 20 and 1000 TW/cm^2 like in [3, 18]. Three Bessel-Gauss beams with different diameters d_0 (distance between the first zeros of the Bessel function in Eq. (7)) and a 20 μm in length in vacuum are considered and presented in Table 1. The simulated Bessel–Gauss length is ten times smaller than the typical Bessel–Gauss length used in experiments [3, 18] due to computational constraints. However, this length is enough to observe modifications of the matter which differ from traditional Gaussian pulses and to capture the main physical processes at play.

The Bessel–Gauss beams propagate inside fused silica target [35, 36] with initial solid density $\rho_0 = 2.2$ g/cm^3, $U_g = 9$ eV, $\tau_r = 150$ fs, $\nu_e = 5$ fs^{-1}, $\tau_{el} = 1$ ps, $C_l = 1.6$ J/cm^3/K, $\chi^{(1)} = 1.11$ and $\chi^{(3)} = 2 \times 10^{-22}$ m^2/V^2. Note that the optical index in the non-ionized matter is different from the vacuum where both Bessel–Gauss beams have been initially defined. In the material, the position of maximum intensity in Bessel–Gauss beams is forward shifted by 11.3 μm along the propagation axis.

The typical value of the α_0 rate in the impact ionization model (see Eq. (4)) is of the order of 1.5 fs^{-1} for fused silica [27, 28]. However, using this value in our simulations with a 60 fs and 800 nm laser pulse, leads to underestimate the absorbed laser energy, and thus the final lattice temperature. For the BG1 beam with I_0 =300 TW/cm^2, the calculated final lattice temperature in the heated matter is in the range of 600 to 800 K. The final lattice temperature should be in the range of the strain and annealing temperatures, **that means** of the order of T_s = 1300 K in fused silica [37], as structure inducing change of the refractive index is experimentally observed for such laser parameters [3]. This low heating in simulation is induced by the sharp evolution of the conduction band electron density leading to a strong screening of the incident laser beam as it will be demonstrated after. On the other hand, removing the impact ionization process in Eq. (4) results to calculated final lattice temperatures of the order of some eV, which is to large. To obtain a temperature of the order of T_s in the heated material, α_0 must be of the order of 0.03 fs^{-1} in our simulation. This decrease of the α_0 value is in agreement with experiment and simulation results [38–40] showing a decrease of the importance of the impact ionization process for laser pulses shorter than 100 fs. This α_0 value is used in all forthcoming simulations.

Figures 1 and 2 present the temporal and spatial evolutions of the electron density and laser intensity distributions in the xy plane for the BG1 and BG3 beams, respectively. The maximum laser peak intensity in vacuum is I_0 = 300 TW/cm^2 in both cases. The laser pulse comes from the left border. The electron densities $\bar{n}_e$ are normalized to the critical electron density $n_c = 1.7 \times 10^{21}$ cm^{-3}. The black and white lines in Figs. 1a and 2a, respectively, correspond to $n_e = 0.5\, n_c$. Larger densities provide an efficient laser energy absorption and reflectivity for the considered laser parameters.

For both Bessel–Gauss beams, the electron density increases slowly during the first 200 fs after the beginning of the laser irradiation, because only photoionization takes place. The electron density in the ionized matter is too low to significantly disturb the incident laser pulse propagation and the Bessel–Gauss beams begins to form in the interference area (around $y = 0$) along the propagation axis. Thereafter, when the laser intensity becomes greater than 0.1 I_0, the energy of the ionized electrons becomes large enough to induce collisional ionization. The electron density in the conduction band sharply increases and a volume of matter where $n_e > 0.5 n_c$ appears.

For the BG1 beam (Fig. 1a), the transverse diameter of the absorption volume where $n_e > 0.5 n_c$, is approximately 1 μm, and its length is 8 μm for $t = 250$ fs. Its shape evolves toward an elongated teardrop shape with 23.2 μm in length and 1.3 μm in maximum diameter at $t = 400$ fs. The maximum electron density is always lower than n_c. Appearance of the absorption volume disturbs the Bessel–Gauss beam formation (Fig. 1b). A large part of the incident beam is

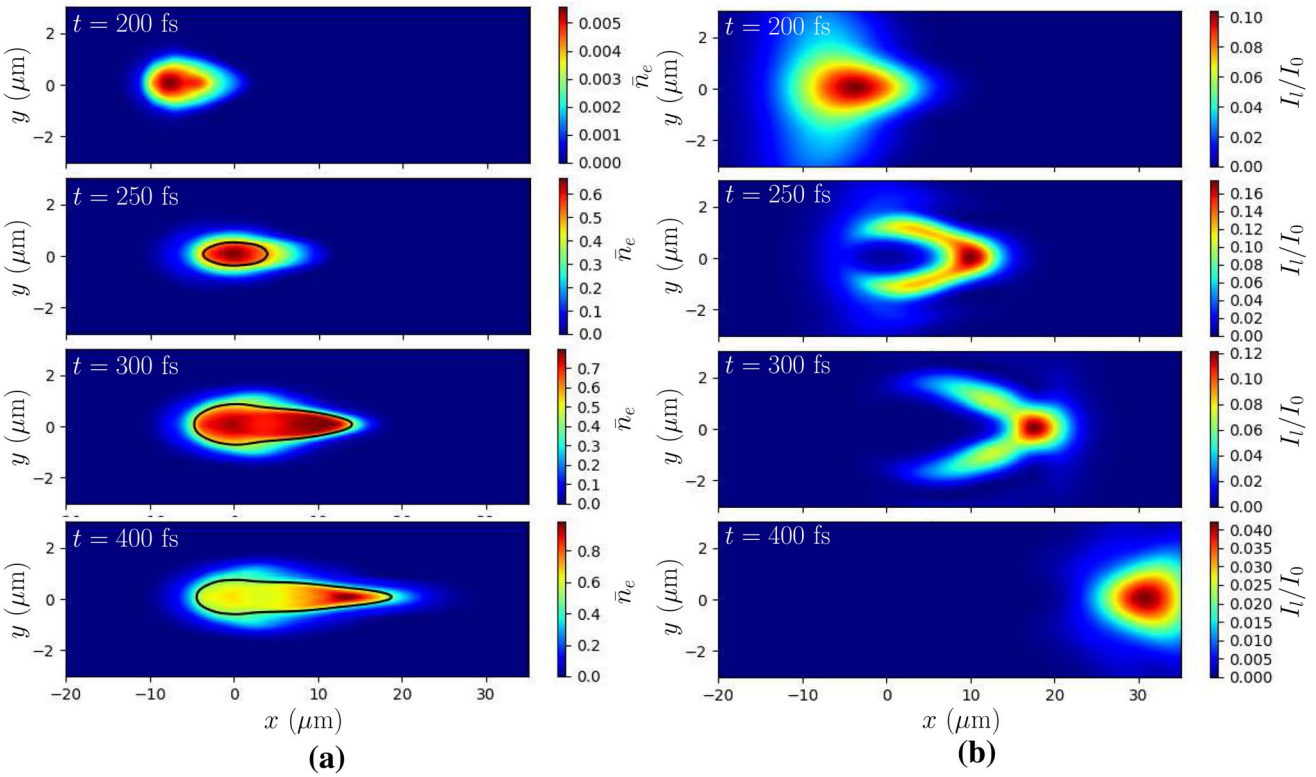

Fig. 1 Spatial and temporal evolutions in the xy plane of the free electron density (**a**) and laser intensity (**b**) in silica for 3.11 μm in diameter Bessel–Gauss beam (BG1). The laser pulse comes from the left border and the laser intensity I_l is normalized to the laser peak intensity I_0 =300 TW/cm^2. The electron density $\bar{n}_e$ is normalized to $n_c = 1.7 \times 10^{21}$ cm^{-3}

Table 1 Diameters d_0, widths of the gaussian term w_0, and angular half apertures θ of the three considered Bessel-Gauss beams with 20 μm in length

Beam	d_0 (μm)	w_0 (μm)	θ (°)
BG1	3.11	2	11.3
BG2	1.8	3.5	19.3
BG3	1.3	5	26.5

absorbed and reflected by the ionized material before to reach the interference area. Only its unperturbed part, which propagates in matter where $n_e < 0.5n_c$, forms a small Bessel–Gauss beam in front of the absorption volume. The laser intensity is maximum in this area but always lower than I_0. This leads to a decrease of tranverse dimension of the absorption volume and to the elongated teardrop shape.

Concerning the BG3 beam (Fig. 2a), the maximum transverse size of the absorption volume where $n_e > 0.5n_c$ increases up to 1.4 μm, that means up to the size of the BG3 beam diameter, at $t = 300$ fs and remains constant after while its length increases up to 30 μm at $t = 400$ fs. At this time, the absorption volume is more homogeneous, thinner and longer than the absorption volume obtained with the BG1 beam. Like in the previous case, the laser beam propagation is also disturbed by the absorption volume formation (Fig. 2b). However, as the θ value is higher in the BG3 beam, the screening effect is lower. The maximum laser intensity in the small Bessel–Gauss beam in front of the absorption volume is always higher than in the BG1 beam leading to stronger electron heating and ionization processes. The maximum electron density increases up to 4.3 n_c. At the same time, the disturbed part of the incident beam induces a laser intensity in the edge of the absorption volume which is large enough to expand its transversal size which becomes of the order of the BG3 beam diameter.

Due to the lower θ value in the BG1 beam, the screening of the incident laser beam induced by the absorption volume formation is higher than with the BG3 beam. The laser intensity in the resulting Bessel–Gauss beam is then smaller leading to a lower material ionization and electron heating. This is confirmed in Fig. 3 where the final calculated lattice temperature corresponding to $T_l = T_e$, is presented in the xy plane for the previously considered Bessel–Gauss beams and $I_0 = 300$ TW/cm^2. The black (for BG1) and white (for BG3) curves correspond to $T_s = 1300$ K. Material modifications or damage can be expected for temperature larger than T_s. For the BG1 beam (top pannel in Fig. 3), only a damaged material volume of 8 μm in length (L_d) where $T_l > T_s$ is obtained. In this heated matter, the averaged temperature $\bar{T}_l$ is 1470 K,

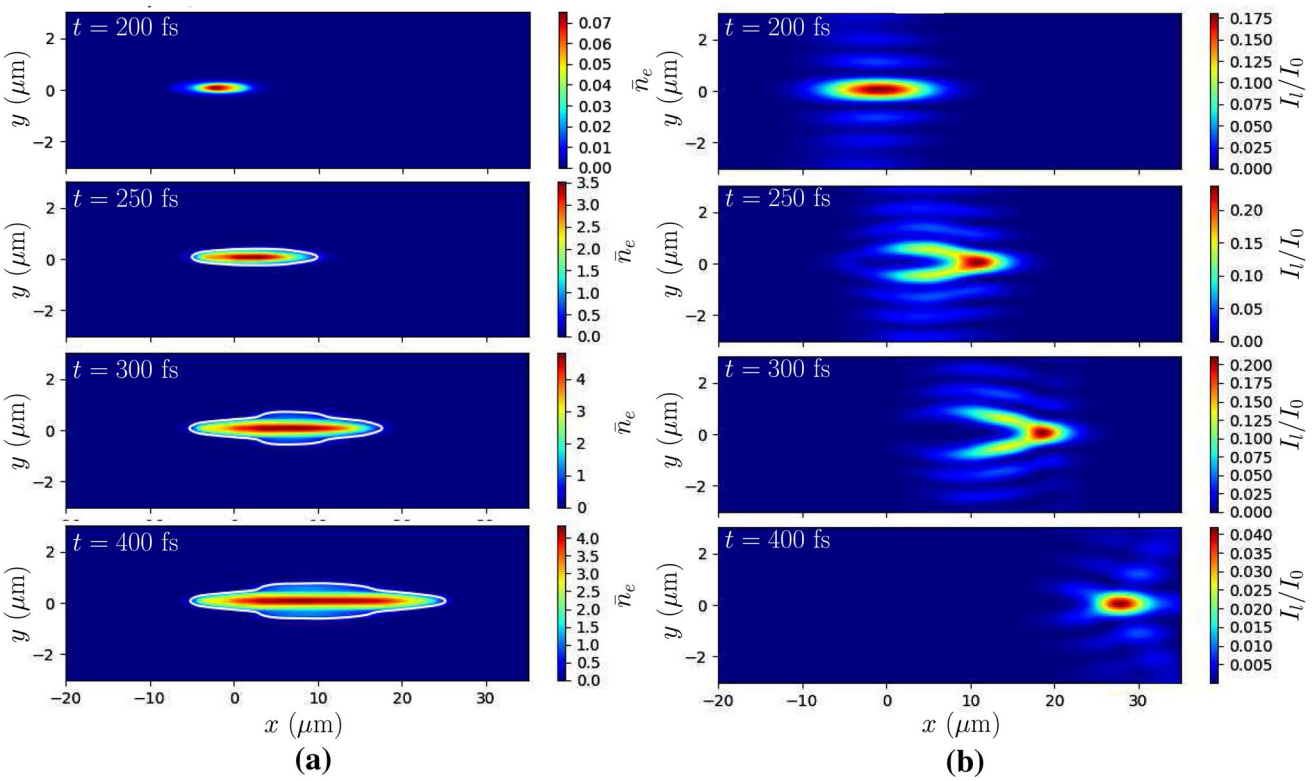

Fig. 2 Spatial and temporal evolutions in the xy plane of the free electron density (**a**) and laser intensity (**b**) in silica for 1.3 μm in diameter Bessel–Gauss beam (BG3). The laser pulse comes from the left border and the laser intensity I_l is normalized to the laser peak intensity I_0 =300 TW/cm^2. The electron density $\bar{n}_e$ is normalized to $n_c = 1.7 \times 10^{21}$ cm^{-3}

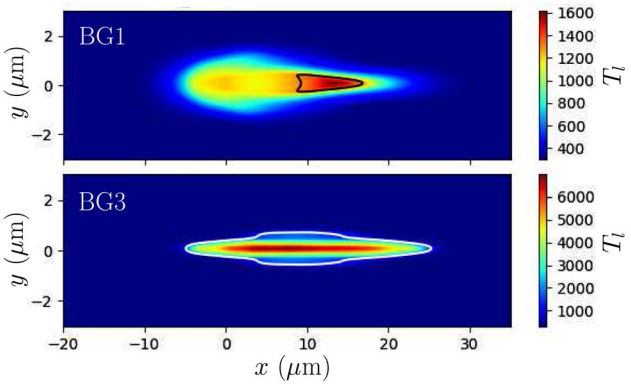

Fig. 3 Final lattice temperature in the *xy* plane for the BG1 (top pannel) and BG3 (bottom pannel) with $I_0 = 300$ TW/cm^2. The black (for BG1) and white (for BG3) lines correspond to $T_l = 1300$ K

and the maximum temperature is 1600 K. It is located between $x = 8.8$ and 16.8 μm, that means in the tail of the absorption volume (see $t = 400$ fs in Fig. 1a). The laser heating is less efficient in the first part of the absorption volume due to its tranverse size which is larger than the laser skin depth induced by the BG1 beam (of the order of 320 nm for $n_e = 0.5\, n_c$). For the BG3 beam (bottom pannel in Fig. 3), the temperature is greater than T_s in a length L_d of 30 μm corresponding to the absorption volume at $t = 400$ fs in Fig. 2a. The maximum temperature is 6900 K and $\bar{T}_l = 5600$ K, larger than temperatures obtained with the BG1 beam. With the same I_0 value, the final modifications of the material will be more significant with a higher θ value. This was also obtained with the BG2 beam (not shown). For $I_0 = 300$ **TW/cm**^{2}, the spatial and temporal evolutions of the electron density and laser intensity in the target for the BG2 beam are quite similar to those presented for the BG3 beam, except that the absorption volume is larger with the BG2 beam, and therefore, the final lattice temperature is lower ($\bar{T}_l = 2800$ **K**).

Figure 4 presents the calculated length L_d of the damaged material volume where $T_l > T_s$ (top pannel) and the averaged temperature $\bar{T}_l$ in this volume of matter (bottom pannel), as a function of the laser peak intensity for the three Bessel–Gauss beams presented in Table 1. In case of BG1 beam, $\bar{T}_l$ becomes higher than T_s for 60 TW/cm^2, and L_d starts to increase sharply with the laser intensity until $I_0 = 100$ TW/cm^2. For these laser intensities, as the maximum transverse size of the absorption volume is of the order of the skin depth, the screening effect is reduced, and the volume of damaged material corresponds to the

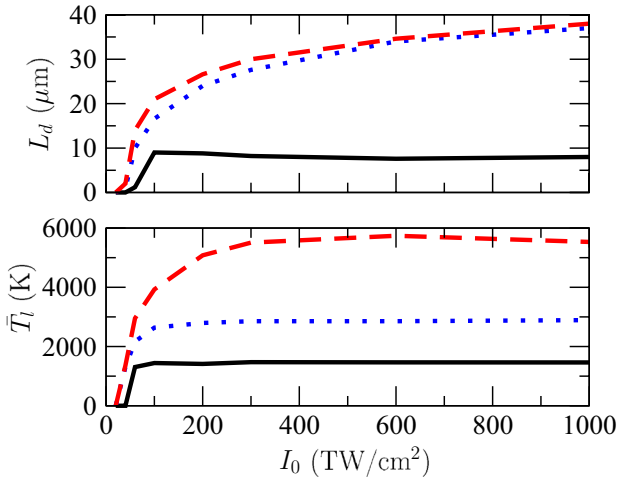

Fig. 4 Evolution of the length of the volume where $T_l > T_s$ (top pannel) and of the averaged temperature in this volume (bottom pannel) as a function of the peak laser intensity, for BG1 (black solid line), BG2 (blue dotted line) and BG3 (red dashed line) beams

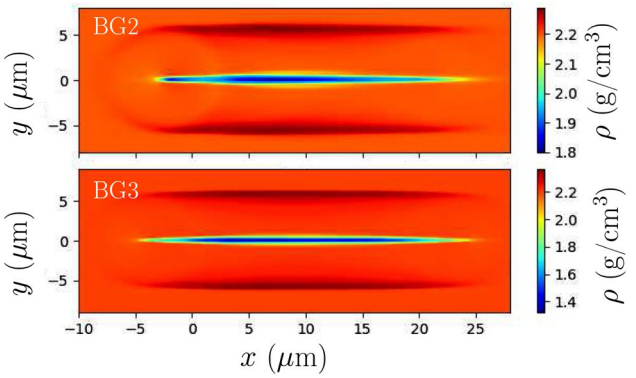

Fig. 5 2D map of the density profile $\rho(x, y)$ at 1 ns after the BG2 and BG3 beam irradiation for $I_0 = 300$ TW/cm^2

absorption volume. For larger intensities, the maximum transverse size of the absorption volume increases, and the damaged material volume corresponds only to the tail of the absorption volume like in Fig. 3. L_d increases slowly while $\bar{T}_l$ remains constant ($\approx$ 1470 K). For the two other beams, the intensity threshold is 40 TW/cm^2. L_d increases always with the laser intensity and tends toward a value close to 45 μm. However, $\bar{T}_l$ increases up to 2800 K for the BG2 beam when the laser intensity reaches 100 TW/cm^2 and remains constant for larger values of I_0. For the BG3 beam, $\bar{T}_l$ increases up to 5600 K until $I_0 = 300$ TW/cm^2. Like with the BG1 beam, the screening effect limits the material laser heating when the laser intensity becomes higher than 100 TW/cm^2 for the BG2 beam and 300 TW/cm^2 for the BG3 beam. However, the undisturbed part of the incident beam is always capable to form a Bessel–Gauss beam ables to heat the matter in front of the absorption volume like in Fig 2b.

These results show that for femtosecond Bessel–Gauss beams, the laser heating is limited to a maximum temperature even if the laser intensity increases. This maximum temperature value increases with the decrease of the Bessel–Gauss beam diameter. Such a behavior can be expected for longer laser pulses. However, since the irradiation time is longer, the absorbed laser energy transfer toward the lattice becomes more efficient before the initiation of the impact ionization process. The electron heating is slower, and the lattice energy becomes higher when the electron density becomes large enough to induce the screening effect. For these Bessel–Gauss beams, it is easier to obtain a maximum temperature higher than the energy threshold for strong material modifications as it was experimentally observed [3].

By using larger Bessel–Gauss beam (BG1), the maximum temperature is slightly larger than the strain temperature. With such Bessel–Gauss beam, one can only expect small structure modifications like refractive index modification in the bulk of SiO_2 target. The material density will be almost unchanged in the heated volume after its relaxation in the surrounding cold solid matter. Using thinner Bessel–Gauss beam allows to heat more efficiently the material along the laser pulse propagation axis due to the larger θ value. However, even if the saturated values of $\bar{T}_l$ are larger than the softening temperature in fused silica ($\approx$ 2000 K), they are too low to induce a pressure of the order of the SiO_2 bulk modulus in the heated matter (75 GPa for silica [7]) and perform voids like in tightly focused conditions with Gaussian beam [41]. For the BG2 and BG3 beams, the heated volume relaxation must be simulated to determine the resulting modifications of the material.

4 Material relaxation

To determine the material modifications after the laser irradiation by using BG2 and BG3 beams, simulations are performed by using the 2D thermo-elasto-plastic model developed in Ref. [23, 24] and implemented in the hydrodynamic CHIC code [21]. This model is based on the standard fluid description which has been augmented by the solid response through the elasto-plastic behavior to include the influence of the surrounding cold solid matter. Despite the simulations are 2D, correct trends are expected due to the system symetry. Deposited laser energy profiles calculated by the ARCTIC code are introduced as initial conditions in the CHIC code by assuming an isochoric heating and using the lattice temperature and pressure distributions deduced from the SESAME table 7386 for fused silica [42]. The calculated density maps $\rho(x, y)$ at $t = 1$ ns after the laser irradiation are presented in Fig. 5 for $I_0 = 300$ TW/cm^2. In both case,

a narrow filament of approximately 25 μm in length and approximately 1 μm in diameter where the density is lower than 2.2 g/cm^3 (initial solid density) and corresponding to the laser heated matter, is observed. It is surrounded by moving compressed areas where the density is higher than the initial solid density, following the sound wave launched from the heated matter. No plastic deformations resulting from the compression waves, i.e., no permanent mechanical deformations of the cold solid matter, are induced in both cases. However, the matter in the filament moves toward metastable liquid states (below the liquid–vapor binodal). Thereafter, a nucleation process leading to formation of vapor bubbles (not included in our simulations) will allow it to reach a liquid-vapor equilibrium state. In the case of the BG3 beam, a uniform channel will probably be induced as the relaxation drive the matter toward a metastable state close to the critical point. In the case of BG2 beam, the final structure should be a non-uniform rarefied zone.

5 Conclusions

In summary, we have reported simulations of material modifications in the bulk of a dielectric by femtosecond Bessel–Gauss beams. The laser–matter interaction has been described by using a 3D Maxwell solver including the electron dynamics. The relaxation of irradiated material has been simulated by a hydrodynamic code including elasto-plastic behavior of the solid matter. Simulations have shown that the femtosecond Bessel–Gauss beam formation is perturbed by the laser ionized matter inducing a screening effect which leads to limit the laser energy absorption even if the incident laser energy increases. This influence is more important for the Bessel–Gauss beam with larger diameter as the θ value, the angular half aperture of the cone along which the incident gaussian beams are distributed to form the Bessel beam, is lower. For this moderate focusing conditions, the incident gaussian beam propagation is strongly disturbed by the ionized matter before to reach the interference area and form the Bessel–Gauss beam. The resulting absorbed energy in the irradiated matter is too low to induce significant modifications in the material after its relaxation. To obtain such modifications in the femtosecond regime, our results show that the Bessel–Gauss beam must be tighter focused as it was observed in experiments. The θ value becoming higher, the influence of the screening effect on the incident gaussian beam propagation is reduced. For the higher considered θ value, channel formation can be obtained. An other way to overcome the electron screening effect would be to use burst of femtosecond laser pulses with a moderate energy per pulse to limit the ionization effect, and picosecond inter–pulse time delay allowing the electron relaxation process to take place significantly before the next pulse.

Acknowledgements We acknowledge the Aquitaine Regional Council for support and funding via the MOTIF project. This work was granted access to the HPC ressources of TGCC under the allocation A0030506129 made by GENCI and the allocation 2017174175 made by PRACE.

Declarations

Conflict of interest The authors declare that they have no conflict of interest.

References

1. M. Duocastella, C.B. Arnold, Laser Photonics Rev. **6**, 607 (2012)
2. F. Courvoisier, J. Zhang, M.K. Bhuyan, M. Jacquot, J.M. Dudley, Appl. Phys. A **112**, 29 (2013)
3. M.K. Bhuyan, P.K. Velpula, J.P. Colombier, T. Olivier, N. Faure, R. Stoian, Appl. Phys. Lett. **104**, 021107 (2014)
4. J. Lopez, K. Mishchik, B. Chassagne, C. Javaux-Leger, C. Honninger, E. Mottay, R. Kling, in Proceedings of ICALEO pp. 60–69 (2015)
5. R.R. Gattass, E. Mazur, Nat. Photonics **2**, 219 (2008)
6. E.N. Glezer, M. Milosavljevic, L. Huang, R.J. Finlay, T.H. Her, J.P. Callan, E. Mazur, Opt. Lett. **21**, 2023 (1996)
7. E.G. Gamaly, S. Juodkazis, K. Nishimura, H. Misawa, B. Luther-Davies, L. Hallo, P. Nicolai, V.T. Tikhonchuk, Phys. Rev. B **73**, 214101 (2006)
8. J. Durnin, J.J.J. Miceli, J. Eberly, Phys. Rev. Lett. **58**, 1499 (1987)
9. F. Courvoisier, P.A. Lacourt, M. Jacquot, M. Bhuyan, L. Furfaro, J. Dudley, Opt. Lett. **34**, 3163 (2009)
10. P.K. Velpula, M.K. Bhuyan, C. Mauclair, J.P. Colombier, R. Stoian, Opt. Eng. **53**, 076108 (2014)
11. J. Artl, K. Dholakia, Opt. Comm. **177**, 297 (2000)
12. V. Jarutis, R. Paskauskas, A. Stabinis, Opt. Comm. **184**, 105 (2000)
13. M. Bhuyan, F. Courvoisier, P. Lacourt, M. Jacquot, R. Salut, L. Furfaro, J. Dudley, Appl. Phys. Lett. **97**, 081102 (2010)
14. K. Mishchik, R. Beuton, O. Dematteo-Caulier, S. Skupin, B. Chimier, G. Duchateau, B. Chassagne, R. Kling, C. Hönninger, E. Mottay, J. Lopez, Opt. Exp. **26**, 33271 (2017)
15. T. Cizmar, K. Dholakia, Opt. Exp. **17**, 15558 (2009)
16. X. Liu, Q. Li, A. Sikora, M. Sentis, O. Utéza, R. Stoian, W. Zhao, G. Cheng, N. Sanner, Opt. Exp. **27**, 6996 (2019)
17. L. Rapp, R. Meyer, R. Giust, L. Furfaro, M. Jacquot, P.A. Lacourt, J.M. Dudley, F. Courvoisier, Sci. Rep. **6**, 34286 (2016)
18. M. Bhuyan, M. Somayaji, A. Mermillod-Blondin, F. Bourquard, J. Colombier, R. Stoian, Optica **4**, 951 (2017)
19. C. Arnold, S. Akturk, A. Mysyrowicz, V. Jukna, A. Couairon, T. Itina, R. Stoian, C. Xie, J. Dudley, F. Courvoisier, S. Bonanomi, O. Jedrkiewicz, P. Trapan, J. Phys. B: At. Mol. Opt. Phys. **48**, 094006 (2015)
20. I. Thiele, P.G.A. de Martinez, R. Nuter, A. Nguyen, L. Berge, S. Skupin, Phys. Rev. A **96**, 053814 (2017)
21. J. Breil, S. Galera, P.H. Maire, Comput. Fluids **46**, 161 (2011)
22. P.H. Maire, R. Abgrall, J. Breil, R. Loubere, B. Rebourcet, J. Comput. Phys. **235**, 626 (2013)
23. R. Beuton, B. Chimier, J. Breil, D. Hebert, P.H. Maire, G. Duchateau, J. Appl. Phys. **122**, 203104 (2017)
24. R. Beuton, B. Chimier, J. Breil, D. Hébert, K. Mishchik, J. Lopez, P. Maire, G. Duchateau, Appl. Phys. A **124**, 324 (2018)
25. C. Mézel, L. Hallo, A. Bourgeade, D. Hébert, V.T. Tikhonchuk, B. Chimier, B. Nkonga, G. Schurtz, G. Travaillé, Phys. Plasmas **15**, 093504 (2008)

26. L.V. Keldysh, Sov. Phys. JETP **20**(5), 1307 (1965)
27. B.C. Stuart, M.D. Feit, S. Herman, A.M. Rubenchik, B.W. Shore, M.D. Perry, Phys. Rev. B **53**, 1749 (1996)
28. J.R. Peñano, P. Sprangle, B. Hafizi, W. Manheimer, A. Zigler, Phys. Rev. E **72**, 036412 (2005)
29. K. Yee, IEEE Trans. Antennas Propag. **14**, 302 (1966)
30. J.P. Berenger, J. Comput. Phys. **114**, 185 (1994)
31. J.P. Berenger, J. Comput. Phys. **127**, 363 (1996)
32. F. Gori, G. Guattari, C. Padovani, Opt. Commun. **64**, 491 (1987)
33. I. Thiele, S. Skupin, R. Nuter, J. Comp. Phys. **321**, 1110 (2016)
34. P.A. González, G. de Martínez, B. Duchateau, R. Chimier, I. Nuter, S. Skupin. Thiele, V.T. Tikhonchuk, Phys. Rev. A **98**, 043849 (2018)
35. B. Chimier, O. Utéza, N. Sanner, M. Sentis, T. Itina, P. Lassonde, F. Légaré, F. Vidal, J.C. Kieffer, Phys. Rev. B **84**, 094104 (2011)
36. N. Bulgakova, R. Stoian, A. Rosenfeld, Q. Elect. **40**, 966 (2010)
37. N. Bulgakova, V. Zhukov, S.V. Sonina, Y. Meshcheryakov, J. Appl. Phys. **118**, 233108 (2015)
38. A. Kaiser, B. Rethfeld, M. Vicanek, G. Simon, Phys. Rev. B **61**, 11437 (2000)
39. A.Q. Wu, I.H. Chowdhury, X. Xu, Phys. Rev. B **72**, 085128 (2005)
40. F. Queré, S. Guizard, P. Martin, Europhys. Lett. **56**, 138 (2001)
41. S. Juodkazis, K. Nishimura, S. Tanaka, H. Misawa, E.G. Gamaly, B. Luther-Davies, L. Hallo, P. Nicolai, V.T. Tikhonchuk, Phys. Rev. Lett. **96**, 166101 (2006)
42. J. Boettger, Sesame equation of state number 7386, fused quartz. Tech. rep., Los Alamos National Laboratory Report LA-11488-MS (1989)

Publisher's Note Springer Nature remains neutral with regard to jurisdictional claims in published maps and institutional affiliations.